Nuclear Engineering and Technology 51 (2019) 1279–1288

Contents lists available at ScienceDirect

Nuclear Engineering and Technology

journal homepage: www.elsevier.com/locate/net

Original Article

Topology optimization on vortex-type passive fluidic diode for advanced nuclear reactors

Do Kyun Lim, Min Seop Song, Hoon Chae, Eung Soo Kim*

Seoul National University, 559 Gwanak-ro, Gwanak-gu, Seoul, South Korea

ARTICLE INFO

Article history:
Received 7 October 2018
Received in revised form
17 February 2019
Accepted 24 March 2019
Available online 26 March 2019

Keywords:
Vortex-type fluidic diode
Topology optimization
CFD
Flow visualization

ABSTRACT

The vortex-type fluidic diode (FD) is a key safety component for inherent safety in various advanced reactors such as the sodium fast reactor (SFR) and the molten salt reactor (MSR). In this study, topology optimization is conducted to optimize the design of the vortex-type fluidic diode. The optimization domain is simplified to 2-dimensional geometry for a tangential port and chamber. As a result, a design with a circular chamber and a restrictor at the tangential port is obtained. To verify the new design, experimental study and computational fluid dynamics (CFD) analysis were conducted for inlet Reynolds numbers between 2000 and 6000. However, the results show that the performance of the new design is no better than the original reference design. To analyze the cause of this result, detailed analysis is performed on the velocity and pressure field using flow visualization experiments and 3-D CFD analysis. The results show that the discrepancy between the optimization results in 2-D and the experimental results in 3-D originated from exclusion of an important pressure loss contributor in the optimization process. This study also concludes that the junction design of the axial port and chamber offers potential for improvement of fluidic diode performance.

1. Introduction

The fluidic diode (FD) is a simple, passive flow control device designed to create a small flow resistance in the forward flow direction and a large flow resistance in the reverse flow direction. It is applied in advanced nuclear reactors such as the hybrid loop-pool type sodium-cooled fast reactors (SFRs) and fluoride-salt-cooled high-temperature reactors (FHRs). In these reactors, the FD plays an important role in implementing the passive core cooling system by restricting flow according to the operational condition [1,2].

The role of the FD in the advanced reactors is shown in Fig. 1 and Fig. 2. The FD is connected to this system to control the flow paths through the system. In normal operation, the reactor core is cooled by forced convection, and flow bypass to the decay heat removal system is restricted by the FD. However, when the pump fails, the reactor core is cooled by buoyancy-driven natural circulation flow. In this case, the FD allows flow to the PHX with low flow resistance and sufficient mass flow rate [1,2].

The vortex-type FD is a simple passive fluidic diode design that consists of a disc-shaped chamber and cylindrical axial and tangential ports, as illustrated in Fig. 3. This device generates a large flow resistance by creating a strong vortex across the chamber in reverse flow. In forward flow, the flow is smooth with a radial flow distribution and the device generates a small flow resistance. This concept has been proposed in many previous research studies due to its simplicity, robustness and ease of maintenance [1,3].

Previously, several experimental and numerical studies were conducted to understand and improve the existing vortex-type FD design. In an early stage of research by Priestman, application of the vortex-type FD was mainly focused on reverse flow [4]. In this study, the design factors affecting the pressure drop in reverse flow were investigated by experiments. Thereafter, the vortex-type FD was studied from various additional perspectives. Chikazawa et al. proposed modification of the tangential port of the FD by targeting the 50 MW SFRs and studied its characteristics using a full-scale experiment [5]. Kulkarni et al. proposed a new design of the vortex-type FD and investigated its performance by experimental study and CFD analysis [6,7]. The flow characteristics inside the vortex-type FD were also investigated by several researchers [8,9]. In those studies, detailed CFD analyses were used to identify the vortex transition, recirculation zone, etc. The most recent study was conducted by Shin et al., in which the axial port of the FD was numerically optimized, and a large performance improvement was demonstrated by CFD analysis [10].

Topology optimization is a mathematical method that optimizes material distribution in a given design domain [11]. Unlike shape

* Corresponding author.
E-mail address: kes7741@snu.ac.kr (E.S. Kim).

https://doi.org/10.1016/j.net.2019.03.018

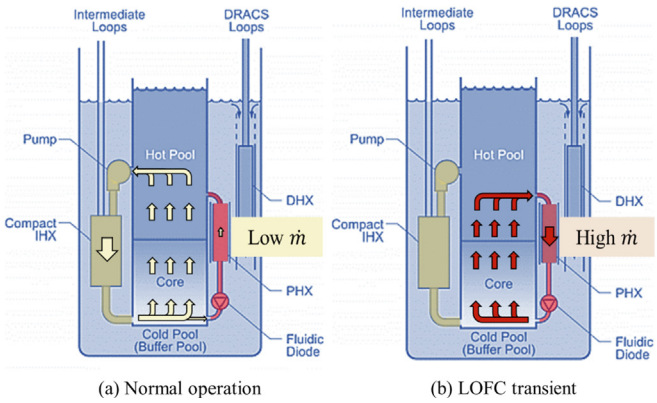

Fig. 1. Flow paths for primary coolant in hybrid loop-pool type SFRs.

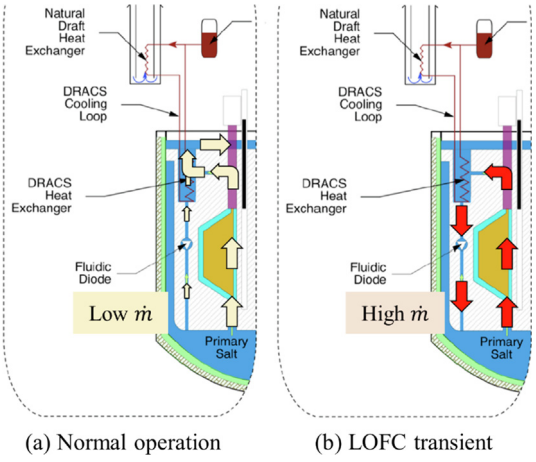

Fig. 2. Flow paths for DRACS facility in FHRs.

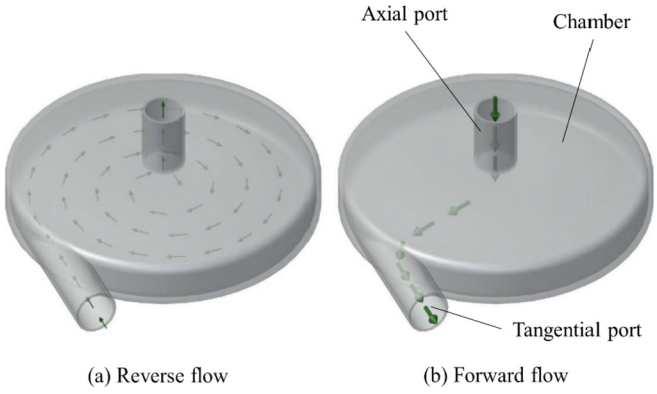

Fig. 3. Flow configuration of vortex-type fluidic diode.

optimization and size optimization, the advantage of the topology optimization is that it does not deal with predefined design parameters but can provide any shape within the design domain. Because of this large degree of freedom, the topology optimization is mostly used at the conceptual design level. Generally, topology optimization uses a finite element method (FEM) and the design is optimized using either gradient-based methods or generic algorithm. Topology optimization was originally proposed in mechanical and structural engineering and the area of application was extended to the fluid flow area to minimize the power dissipated in the fluid [12]. After extension to fluid mechanics, topology optimization was used to design various flow devices [13,14]. Studies that implement the topology optimization technique in a turbulence model are also in progress [15]. Due to the free forms of the final shape, the design is often difficult to manufacture using conventional manufacturing techniques. For that reason, the design obtained from topology optimization is often fine-tuned for manufacturability.

In this study, fluidic diodes are optimized using the topology optimization method and are verified via experiments and numerical simulations. Among the existing studies, an example exists in which topology optimization is applied to the axial port of the vortex-type FD [10], but no studies have yet been performed on the vortex-type FD main body (chamber and tangential port).

2. Topology optimization for vortex-type fluidic diode

Compared with conventional optimization, the main difference in topology optimization is the use of the density function (γ). The density function is a function of the material distribution of the entire design domain and is used as a design variable during the topology optimization process. The density function is defined in each grid, and the value must be discrete, ideally '0' (solid region) or '1' (fluid region). In practice, the density function is defined as a continuous function varying from 0 to 1 for use of a gradient-based numerical optimization algorithm. The main advantage of using density function is its high degree of freedom, resulting in a higher probability of performance enhancement. However, there are several technical difficulties in using the density function [10]. First, optimized solution is sensitive to the problem set-up and initial condition. If it is ill-conditioned, the problem may not converge into a global optimum but into a local optimum. Second, since the grid size is initially fixed, boundary layers cannot be resolved near the walls for each optimization steps. It makes us difficult to apply topology optimization to turbulent flows. For this reason, we divided the optimal design process into two steps. First, topology optimization was conducted in low Reynolds number condition. Then, the obtained design was evaluated for higher Reynolds number condition using experiments and CFD analysis.

2.1. Basic equations

In general topology optimization for fluid flow, the Navier-Stokes equation with the incompressible assumption is generally applied with selected modification, as follows.

$$\rho(\nabla \cdot \overline{u}) = 0 \tag{1}$$

$$\rho(\overline{u} \cdot \nabla)\overline{u} = -\nabla P + \mu\nabla^2\overline{u} + \overline{f}_d \tag{2}$$

where $\overline{f}_d$ is the additional Darcy friction force. The Darcy friction force term is a function of the density function (γ), and it applies additional flow resistance, as shown below [12].

$$\overline{f}_d = -\alpha\overline{u} \tag{3}$$

In topology optimization, α is adjusted to allow or restrict flow in a certain grid during the optimization process. In this study, the following formulation is applied for α, which is a function of the density function (γ) [12].

$$\alpha(\gamma) = \alpha_L + (\alpha_U - \alpha_L)\frac{q(1-\gamma)}{q+\gamma} \tag{4}$$

In practice, the value of α_L is set to zero, and the value for α_U is set to an infinitely large value. The q is a parameter to control convexity of the α. The variable q affects convergence and stability of the optimization process, but does not affect the final results.

As mentioned above, in principle, the density function should have discrete value of 0 for the solid region and 1 for the fluid region, but it is practically assumed in the form of a continuous function from 0 to 1 for numerical stability of the optimization process with a gradient-based algorithm. Because of this assumption, the intermediate region, where the density function value is between 0 and 1, can be contained in the design domain. To obtain the flow variables in all regions (fluid, solid, and intermediate), the Darcy friction force term was added to the momentum equation. The Darcy friction force term changes the momentum equation according to the density function value.

In the fluid region ($\gamma = 1$), α and $\bar{f}_d$ become zero, making the momentum equation the same as the general Navier-Stokes equation, as shown below.

$$\rho(\overline{u}\cdot\nabla)\overline{u} = -\nabla P + \mu\nabla^2\overline{u} \tag{5}$$

In the solid region ($\gamma = 0$), α becomes infinitely large, suppressing flow passing through the solid region.

$$\overline{u} = 0 \tag{6}$$

In the intermediate region ($0 < \gamma < 1$), α has an intermediate value between zero and α_U. Thus the equation has the form of the Brinkman equation for flow passing through porous media.

$$\rho(\overline{u}\cdot\nabla)\overline{u} = -\nabla P + \mu\nabla^2\overline{u} - \alpha\overline{u} \tag{7}$$

2.2. Optimization formulation

In this study, the performance of the vortex-type FD is quantified using the diodicity (Di). This parameter is defined as the ratio of the pressure drop in reverse flow to forward flow for the same inlet Reynolds number.

$$\mathrm{Di} = \frac{\Delta P_{reverse}}{\Delta P_{forward}} \tag{8}$$

This formulation indicates that larger diodicity supplies better performance. Thus, the inversion of diodicity was set as the objective function (Φ) for numerical optimization. The following summarizes a set of equations and constraints considered in this study.

$$\min\left(\Phi = \frac{1}{Di}\right) \tag{9}$$

Subject to:

$$\rho\left(\nabla\cdot\overline{u}_f\right) = 0 \tag{10}$$

$$\rho\left(\overline{u}_f\cdot\nabla\right)\overline{u}_f = -\nabla P_f + \mu\nabla^2\overline{u}_f - \alpha(\gamma)\overline{u}_f \tag{11}$$

$$\rho(\nabla\cdot\overline{u}_r) = 0 \tag{12}$$

$$\rho(\overline{u}_r\cdot\nabla)\overline{u}_r = -\nabla P_r + \mu\nabla^2\overline{u}_r - \alpha(\gamma)\overline{u}_r \tag{13}$$

$$0 \le \gamma \le 1 \tag{14}$$

The parameter values of α_U and q are controlled for convergence and stability of optimization algorithm. Detailed parameter values will be discussed in Section 2.3. This optimization formulation is implemented using the finite element method (FEM), and the SNOPT algorithm is used to solve the problem [16]. COMSOL Multiphysics code is applied for modeling and optimization [17,18].

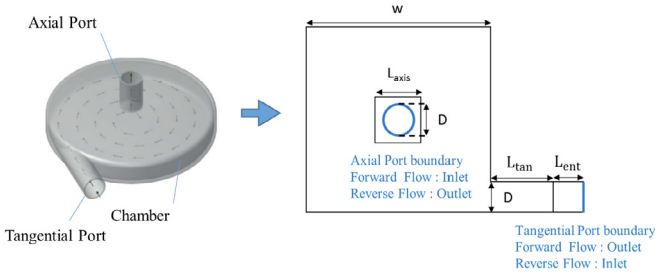

(a) Vortex Diode (b) Design domain and Boundary condition

Fig. 4. 2-D Optimization geometry and boundary conditions.

2.3. Topology optimization on a vortex-type fluidic diode

In this study, topology optimization was conducted for the tangential port and the chamber of the vortex-type FD. Conceptually, the topology optimization can be applied in 3-D domains. However, it requires large computational cost and the solution can be easily converged to local minimum solutions due to its large degree of freedom. To avoid these technical difficulties, the optimization problem was simplified into 2-D domain, as shown in Fig. 4. The domain of the chamber was implemented as a square to offer additional geometrical flexibility during optimization. The tangential port was implemented as a straight pipe, and the axial port was assumed as the central hole of the chamber. All geometrical parameters were expressed in dimensionless form with respect to the tangential port diameter (D). The chamber aspect ratio (w/D) was set to 6.0, and the axial port diameter was set the same as the diameter of the tangential port (D) based on previous studies [4,6]. The central hole of the chamber and the end of the straight pipe were set as the inlet and outlet for fluid flow, according to the flow mode. Square regions in the vicinity of inlet and outlet were excluded from the design domain for numerical stability.

The optimization parameters were also carefully selected to avoid local minimum solutions. As mentioned above, the values of the parameter q are adjusted for numerical stability and convergence [12]. With smaller q value, optimization algorithm can avoid the local minimum solution but the solution has many grids with intermediate density ($0 < \gamma < 1$). In contrast, with larger q value, the optimization algorithm can suppress grids to have intermediate density but it is more likely to acquire local minimum solution. Thus, optimization is conducted in a two-step procedure. In first step, the algorithm searches initial condition with small q value. Then, in second step, the algorithm searches optimal solution with larger q value using initial condition obtained at first step. In this

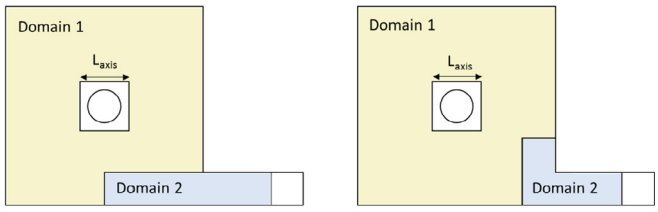

(a) Domain division A (b) Domain division B

Fig. 5. Divided design domain.

study, the parameter value of q = 0.1 is used in the first step, and the parameter value of q = 0.2 is used in the second step. For practical purposes, the parameter value of $\alpha_U = 1 \times 10^8$ is used.

As shown in Fig. 5, the entire design domain was divided into two subdomains. Domain-1 contains the chamber region, and domain-2 contains the tangential port and junction. In the first optimization step, the domain-2 was excluded from optimization, and only domain-1 was optimized with the zero (fluid) initial density function condition. Then, this result was applied as an initial condition for optimizing the whole domains. From this separated optimization procedure, more consistent solution convergence has been achieved. To check the sensitivity of the domain division, optimization was conducted with two different domain divisions.

The whole geometry was discretized with a triangular unstructured grid, as shown in Fig, 6. As mentioned above, it is difficult to perform topology optimization in a turbulent regime because no appropriate boundary layers can be generated for each intermediate design during optimization. For this reason, topology optimization in this paper is generally performed based on low Reynolds number laminar flow condition (Inlet Re = 300). Because topology optimization has been conducted without turbulence models, experiments and CFD simulations were performed to evaluate the optimum designs. This issue is discussed further in the following chapters.

The optimization results and their performance are summarized in Fig. 7. It can be observed that both results have similar features, i.e., circular shape of the chamber, restrictor in the tangential port, and smooth connection between the tangential port and chamber. According to the analysis results, the newly formed structure at the connection area did not affect the pressure drop due to the Coanda effect in the forward direction flow, but it acts as flow resistance in the backward direction, thereby preventing the entry of the flow [10]. It can also be considered that energy dissipation by the rotating flow is improved by accelerating the flow entering the chamber due to the narrowed flow path.

2.4. New design of a vortex-type fluidic diode

Based on the topology optimization results from the previous section, the design of the fluidic diode was obtained as follows. The chamber and the tangential port were designed based on the topology optimization result, as shown in Fig. 8. Overall, the shape and geometry of the new design appear similar to those of the original design except for the connection between the port and the chamber. In the new design, a fin-shape structure is added to restrict flow in the reverse direction. The axial port design was maintained the same as in the existing design because the axial port is not involved in the optimization domain. The major parameters of the new design are listed in Table 1.

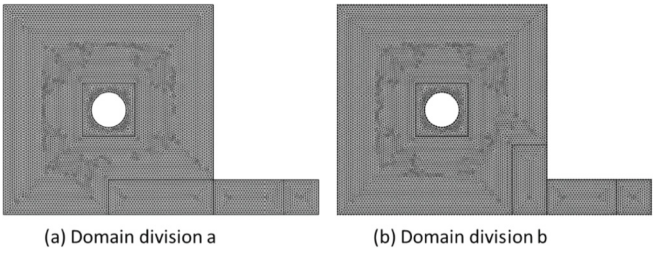

Fig. 6. Grid for design domain.

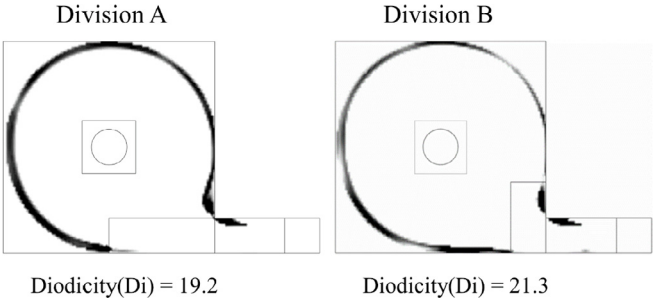

Fig. 7. Optimization results.

3. Experimental study

3.1. Experimental setup

To evaluate the performance of the optimized fluidic diode in this study, experiments were performed. Two different designs were tested: the reference design and the new design. The differences between the two designs are illustrated in Fig. 9. The chamber aspect ratio of the reference design was set to 6.0, which is the same as that of the new design. Compared with the reference design, the new design has two major design modifications: a deformed chamber shape and an additional fin-shaped obstacle in the tangential port.

Fig. 10 shows the schematic drawing for the test loop. The entire loop was designed to measure the pressure drop and velocity profiles. The test section was submerged in the reservoir for flow visualization. The refractive indices between the test section and the fluid were matched to remove optical distortion. In the experiment, flow was circulated by a centrifugal pump and was monitored by two flow meters. Pressure drops were measured between the inlet and the outlet ports of the test section using two differential pressure transmitters, since the pressure drops for the forward and reverse flows show highly different ranges. The turbine flow meter had less than ±2% measurement error. The differential pressure transmitter had a 0–3 bar measurement range with ±0.25% error for the reverse flow, and the other differential pressure transmitter for forward flow had 0–100 mbar range with ±0.075% error.

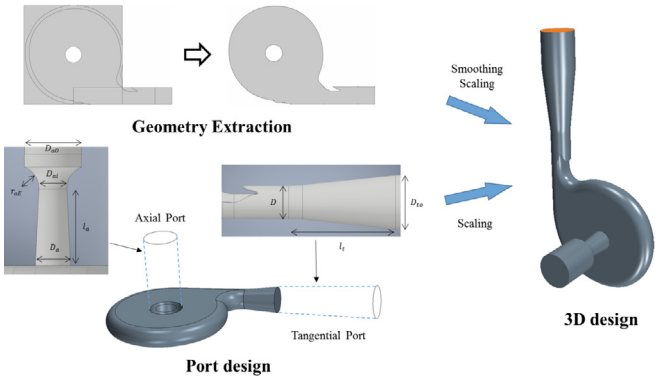

Fig. 8. New Vortex-type fluidic diode design.

Table 1
Geometrical parameters for new design.

Parameters	Values
Chamber height (h/D)	1
Tangential port diffuser length (l_t/D)	3.12
Tangential port outer diameter (D_{tO}/D)	1.63
Axial port diameter (D_A/D)	1
Axial port length (l_a/D)	2.2
Axial port inner diameter (D_{ai}/D)	0.8
Axial port connection radius (r_{aE}/D)	0.64
Axial port outer diameter (D_{aO}/D)	1.636

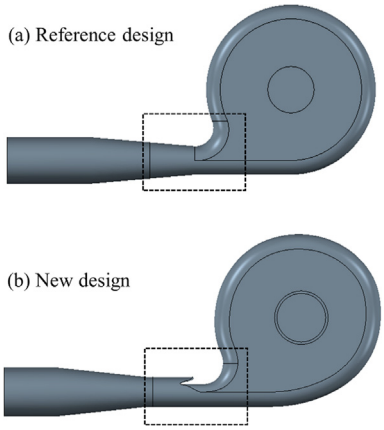

Fig. 9. Comparison of reference design and new design.

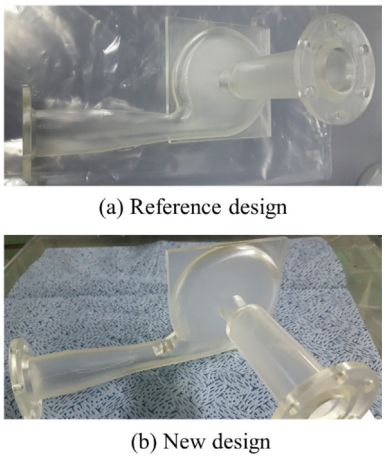

Fig. 11. Photo of the test sections manufacture by SLA 3-D printing.

The experiment was conducted at 20°C and ambient pressure. In this condition, the fluid density was 915 kg/m^3, and the viscosity was 0.004 kg/m·s. In the experiments, the volumetric flow rate ranged from 5.685 to 17.054 LPM, which corresponds to inlet Reynolds number from 2043 to 6128. The flow rates were selected based on the typical operation conditions of some reference reactors. In FHRs, the inlet Reynolds number of a FD ranges between 2000 and 3000 [19]. In hybrid loop-pool type SFRs, the inlet Reynolds number of a FD becomes more than 1×10^5 [1]. In this study, the experimental condition is more close to those of FHRs.

Fig. 11 shows the photos of the manufactured test section. In this test section, a guide plane was added to specify the central line of the chamber. The diameter of the tangential port (D) for each test section was 13.5 mm, and the thickness of the test section wall is set to 3 mm. The diameter of the tangential port was determined to be the same as the reference design in the literature [19]. To construct a transparent test section without shape distortion, test sections were produced using the stereolithography (SLA) technique. The test sections were fabricated having 0.5 mm additive layers aligned to the camera with a 45° angle to avoid laser light reflection and refraction between additive layers [19].

The PIV method was chosen to measure the velocity field. As mentioned above, the optical distortion was minimized by matching the refractive indices between the models and the fluid. The model was manufactured via 3-D printing with a TSR-829 epoxy type resin, which is transparent. The refractive index of this material was 1.514 for the 523 nm laser light used in PIV measurement. To match the refractive indices, two oil-based fluids were mixed: anise seed oil and light mineral oil [20]. In this study, the proportions of anise and mineral oils were 0.402:0.598. The flow inside the vortex-type fluidic diode was measured using a particle image velocimetry (PIV) system (ILA, Germany). This system consists of a 532 nm Nd:Yag laser and a CCD camera with 2 megapixels and a 14-bit range. The camera field of view is 80 × 60 mm, and the resolution is 1600 × 1200 pixels. Silver-coated hollow glass spheres with a 15 μm diameter were selected as seed particles. In this study, the flow was visualized only for the reverse flow. Fig. 12 shows the measurement plane, which is horizontal through the center of the chamber. Images were captured at various time intervals from 50μs to 400μs to resolve the strong vortex flow in the chamber.

3.2. Experimental results

Fig. 13 shows the change in the measured pressure drop with respect to the inlet Reynolds number. In this figure, the y-axis denotes the Euler number, which expresses the relationship between a

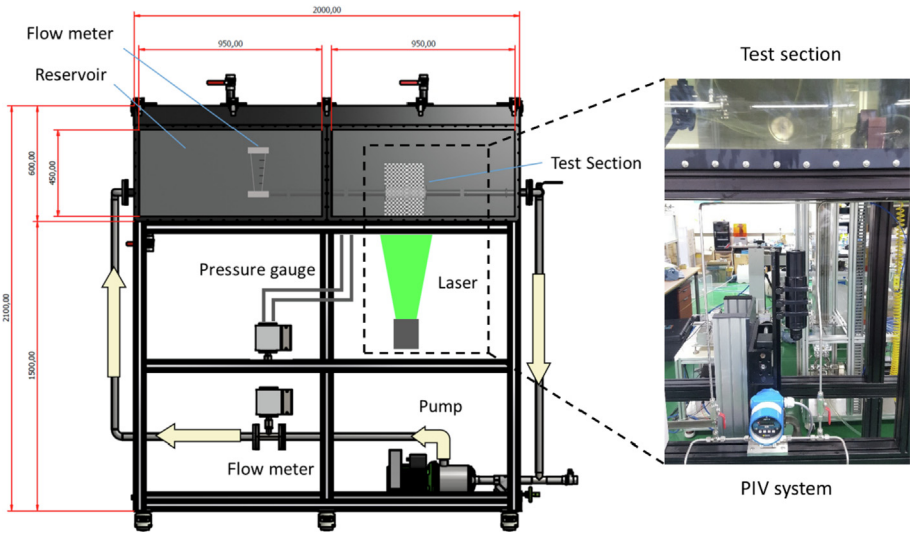

Fig. 10. Schematic drawing for test loop.

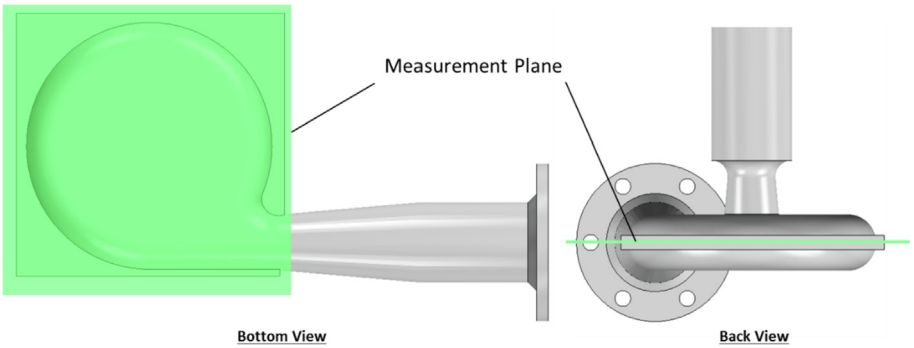

Fig. 12. Measurement plane for flow visualization.

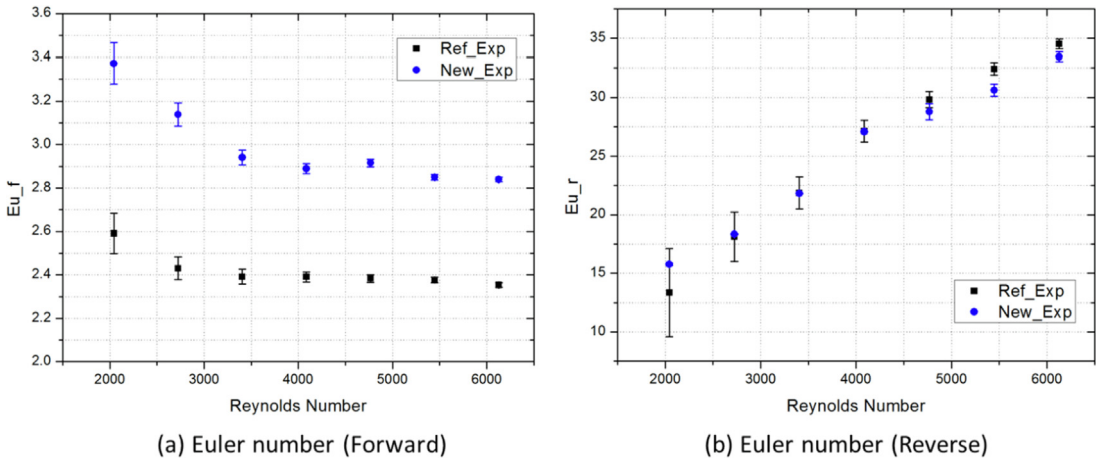

Fig. 13. Experimental results for pressure drop measurement.

local pressure drop caused by a restriction and the kinetic energy ($\mathrm{Eu} = \Delta p/\rho u^2$). According to the experiment, the new design showed higher flow resistance than the reference design in forward flow. However, both designs have similar flow resistance in reverse flow. Therefore, it can be said that the new design has lower performance than the reference design, as shown in Fig. 14. In addition, the tendency increases as the inlet Reynolds number increases. This result was contrary to expectation, meaning that the new structure at the connection between the chamber and the tangential port played a role in reducing the performance in the 3-D geometry. Therefore, to understand the cause of this discrepancy, velocity field analysis via flow visualization experiments and pressure field analysis using the CFD analysis results were performed in this study.

Fig. 15 presents an example of velocity field measurement in a fluidic diode using PIV. In this experiment, it was observed that strong vortices were generated in both designs and that the vortex centers were not consistent with the geometrical center of the chamber. For more quantitative comparisons, the tangential velocities perpendicular to the radial direction were extracted from the measurement line and compared. The measurement line is a straight line parallel to the tangential port passing through the vortex center. Fig. 16 shows the comparisons of tangential velocities in terms of normalized distance from the vortex center. In reverse flow, the flow inside the chamber can be divided into two regions where the tangential velocity becomes linearly proportional to the distance and the tangential velocity is inversely proportional to distance. The first region is known as the forced vortex region, and the second region is known as the free vortex region [7,9]. In both designs, flow inside the chamber is well divided into the free vortex region and forced vortex region, and a local peak is observed at the

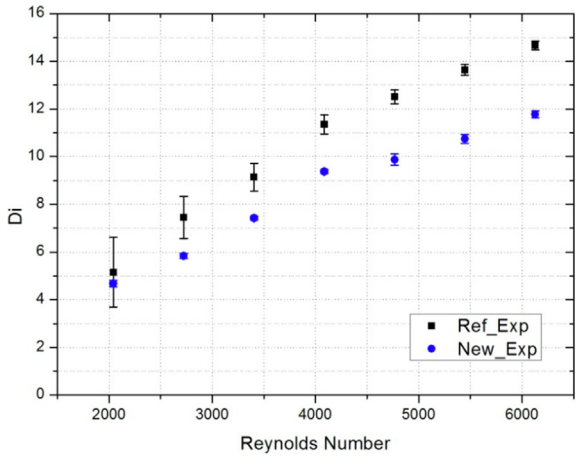

Fig. 14. Diodicity comparisons.

edge of chamber. The reason for this peak is flow with a parabolic velocity profile, which comes from the tangential port. This local peak decreases as flow from the tangential port approaches turbulent flow. The new design has a higher local peak value at the edge of chamber throughout the entire range of Reynolds numbers because the obstacle in the tangential port reduces the cross-sectional area of the port. Despite the higher local peak at the edge of chamber, both designs have similar velocity values near the vortex center. This phenomenon means that velocity change at the chamber edge has a minimal effect on the velocity near the vortex center.

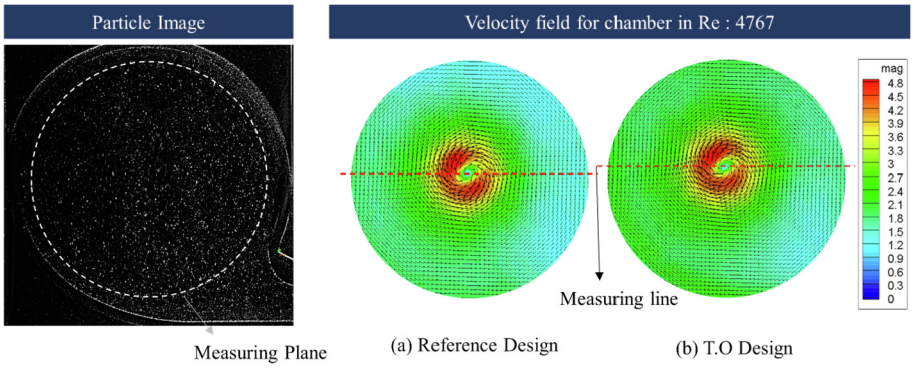

Fig. 15. PIV measurement for fluidic diode models (reverse flow).

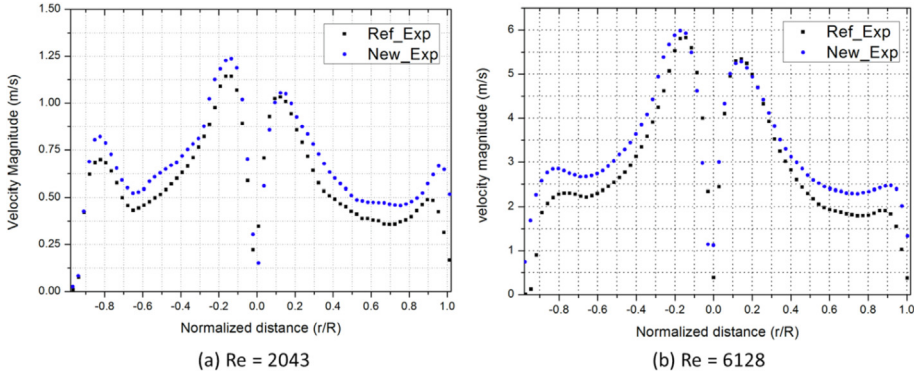

Fig. 16. Comparison of tangential velocities in measurement line.

4. CFD analysis

In the previous section, it was found that the new design optimized in the 2-D domain exhibited lower performance than the reference design, contrary to expectation. To clarify the causes and problems, 3-D CFD analysis was performed in this section, and the pressure distribution and flow characteristics inside the fluidic diode were examined.

4.1. Computational model

The 3-D CFD analysis was conducted for the reference design and the new design. Three inlet Reynolds number cases (Re 2043, 4086, 6128) were selected as analysis condition to cover experimental condition. The 3-D domains with the same size as the test sections were defined. Extensions for the axial port and tangential port were included to supply an entrance length at the inlet and to prevent reverse flow at the outlet. The extension length was determined to be approximately 10D for the axial port and approximately 6D for the tangential port. Unstructured grids with polyhedral elements were generated in the entire core region except for the prism layer near the wall. Fig. 17 shows the geometry and mesh of the models. The thickness of the near-wall mesh was controlled to a y + value less than 1.5 in all analysis conditions. The total number of elements is 1,116,761 for the reference design and 1,205,076 for the new design.

The flow model was applied according to inlet Reynolds number condition. SST-k-ω turbulence model was used when flow is turbulent flow regime. The SST-k-ω is a widely applied, robust, two-equation turbulence model that combines the k-ε and the k-ω model [21]. In the SST-k-ω model, the k-ω model is used in the boundary layer, and the k-ε model is used in the free shear flow. The SST-k-ω model is known to be suitable for prediction of flow separation and an adverse pressure gradient, which might appear in the optimized fluidic diode port. However, it is not guaranteed that the SST-k- ω model is valid for low Re numbers. So, in this study, we also applied other models applicable for low Re numbers. In this model, damping functions are introduced for the coefficient of turbulence model [22]. There are several low-Reynolds turbulence models depending on the types of damping functions and among them, this study used the most common low-Reynolds k-ε model

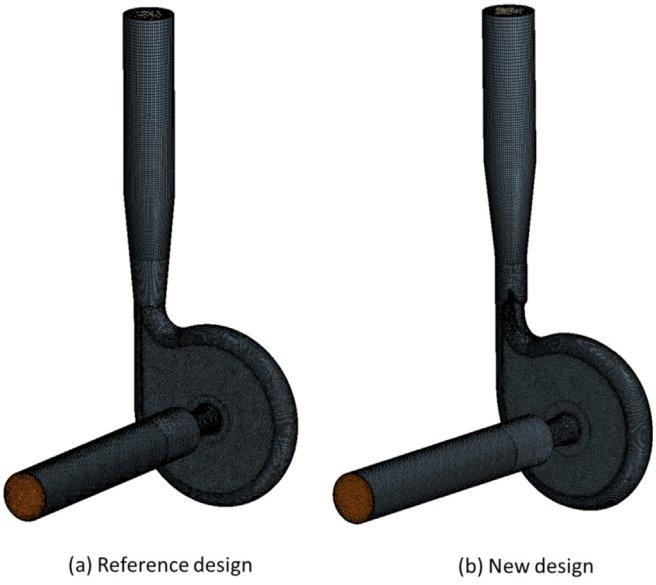

Fig. 17. Grid for CFD analysis.

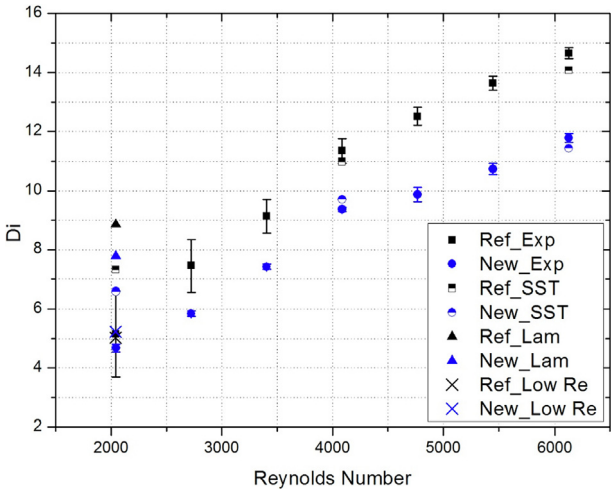

Fig. 18. Comparison of CFD analysis and experimental results (Di).

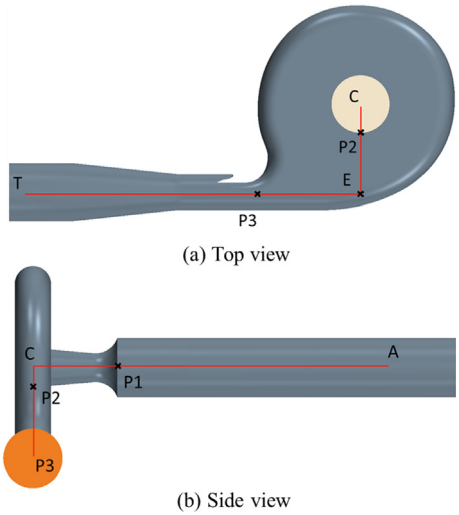

Fig. 19. Hypothetical lines and points for pressure analysis.

[23]. The SST-k-ω model and low-Reynolds k-ε model recommends small y + values for near-wall modeling (y+ ~ 1) because no wall function is used near the wall boundary.

The pressure outlet condition with 0 Pa was applied to the outlet. If only this condition is applied in the reverse flow mode, the circulatory flow generated in the chamber is maintained until the outlet. The circulatory flow in the outlet generates a distribution of pressure, which causes the reverse flow from the outlet. To avoid the reverse flow, a loss coefficient was applied to the outlet. It was reported that the predicted pressure drop result is insensitive to the loss coefficient value [7]. The minimum loss coefficient value to avoid reverse flow was searched for each flow condition. The loss coefficient value ranges from 1 to 3 in forward flow mode, and from 2 to 5 in reverse flow mode. The STAR-CCM + commercial CFD code was applied for the analysis.

5. Results and discussion

To validate the computational model, the 3-D CFD analysis results were compared with the experimental data. Fig. 18 shows comparisons of the diodicities for various Re numbers. As shown in this figure, the CFD results from SST-k-ω model shows very good agreement with the experimental data overall. However, this model didn't predict the experimental results well for the low Re number case (Re = 2043). According to the sensitivity study for turbulence model, the low-Reynolds k-ε model showed very good agreement with the experimental data. For this reason, we used the results from the SST k-w model for high Re numbers (Re = 4086, 6128) and the low Reynolds k-ε model for low Re number (Re = 2043) for detailed analyses and discussions.

Based on the validated model, the pressure distribution and loss were investigated along the flow path. To figure out the contribution of each subpart, the total pressure distribution was observed along a hypothetical line depicted in Fig. 19. The hypothetical line passes through the axial port (A-P1), chamber center and junction with the axial port (P1–C–P2), chamber periphery (P2-E-P3), and tangential port (P3-T). The total pressure change along these lines is plotted in Fig. 20. It can be observed that the total pressure distribution has a similar pattern in both designs. In forward flow, significant loss occurs when fluid from the axial port collides with the chamber wall, and moderate loss subsequently occurs by passing through chamber periphery and tangential port. In reverse flow, moderate loss occurs when it creates a vortex in the chamber periphery. Significant loss occurs when the vortex flow suffers from the transition to axial flow in the chamber center and the junction with the axial port. For all designs and flow modes, a major loss of kinetic energy occurs in the chamber center and the junction with the axial port (P1–C–P2).

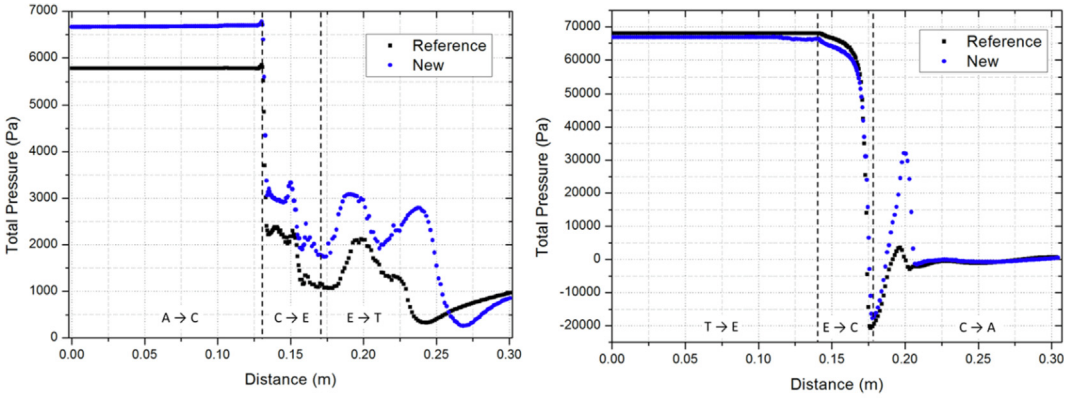

Fig. 20. Total pressure distribution plot along a hypothetical line (Inlet Re: 6128).

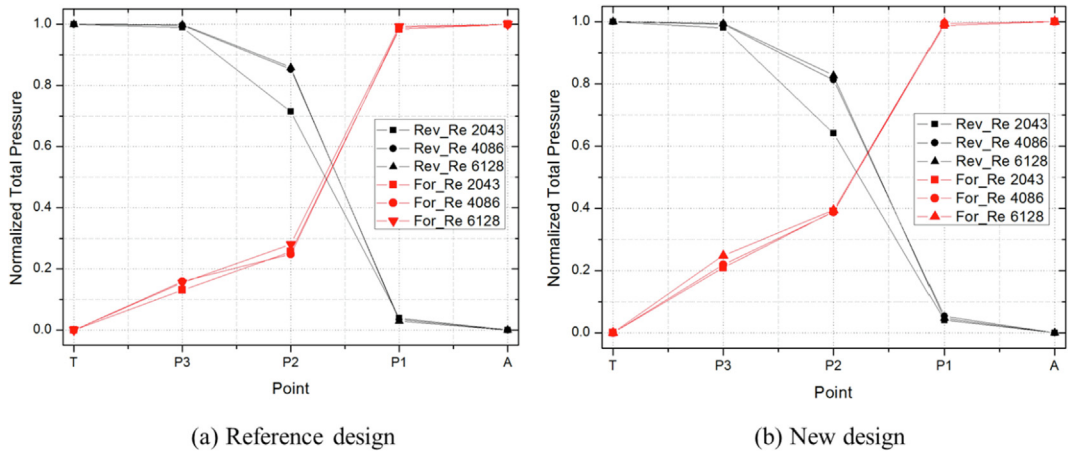

Fig. 21. Normalized total pressure loss between hypothetical points.

To estimate the pressure loss contributions, the pressure loss was normalized to the whole total pressure loss and plotted in Fig. 21. In forward flow, major hydraulic loss occurs in the chamber center and the junction with the axial port (P1–P2). The percentage of loss occurring in this subpart reaches 75% for the reference design and 60% for the new design. Moderate hydraulic loss occurs in the tangential port and chamber periphery (P2–P3, P3-T). In reverse flow, the major hydraulic loss occurs in the chamber center and the junction with the axial port (P2–P1). The percentage of losses occurring in this subpart reaches 83% for the reference design and 78% for the new design. The hydraulic losses occurring in the tangential port (T-P3) and axial port (P1-A) are negligible.

To confirm how modification of the new design affected the pressure drop, the total pressure losses of the reference design and new design are compared from Tables 2–7. After the reference design was changed to the new design, the total pressure loss at the tangential port (T-P3) and chamber periphery (P3–P2) increased in forward flow. For the reverse flow mode, the total pressure loss increased at all subparts except for the chamber center and junction with the tangential port (P2–P1). In general, an additional obstacle in the fluidic diode enhances its didodicity by increasing the pressure drop further in reverse flow than in forward flow. The ratio of the total pressure loss at the tangential port (T-P3) increased more in reverse flow mode than in forward flow mode. Based on this result, it can be observed that modification of the new design has the effect intended in the optimization process. However, the design modification effect in reverse flow becomes insignificant because of the negligible contribution of the tangential port. In contrast, the design modification was effective in forward flow because of the moderate contribution of the tangential port. Therefore, it can be concluded that the discrepancy between the optimization results in 2-D and the experimental results in 3-D are primarily due to exclusion of the important pressure loss contributor in the 2-D optimization process. This result also offers the perspective that the junction design of the axial port and the chamber offers significant potential for improving the fluidic diode performance.

Table 2
Total pressure loss in forward flow mode: inlet Re 2043 condition.

	T - P3	P3 – P2	P2 – P1	P1 - A
Reference	70.711 Pa	67.822 Pa	394.826 Pa	8.455 Pa
New	129.27 Pa	96.507 Pa	370.339 Pa	7.179 Pa
Ratio	1.828	1.644	0.938	0.849

Table 3
Total pressure loss in forward flow mode: inlet Re 4086 condition.

	T - P3	P3 – P2	P2 – P1	P1 - A
Reference	354.486 Pa	199.871 Pa	1160.79 Pa	21.869 Pa
New	556.366 Pa	429.064 Pa	1542.47 Pa	12.711 Pa
Ratio	1.569	2.147	0.929	0.581

Table 4
Total pressure loss in forward flow mode: inlet Re 6128 condition.

	T - P3	P3 – P2	P2 – P1	P1 - A
Reference	717.773 Pa	588.944 Pa	3316.21 Pa	30.164 Pa
New	1343.49 Pa	785.253 Pa	3245.86 Pa	30.024 Pa
Ratio	1.872	1.33	0.979	0.995

Table 5
Total pressure loss in reverse flow mode: inlet Re 2043 condition.

	T - P3	P3 – P2	P2 – P1	P1 - A
Reference	26.806 Pa	746.785 Pa	1833.87 Pa	104.632 Pa
New	63.662 Pa	1118.25 Pa	1986.29 Pa	133.410 Pa
Ratio	2.375	1.497	1.083	1.275

Table 6
Total pressure loss in reverse flow mode: inlet Re 4086 condition.

	T - P3	P3 – P2	P2 – P1	P1 - A
Reference	66.690 Pa	3528.14 Pa	19993.5 Pa	823.582 Pa
New	182.70 Pa	4415.51 Pa	18689.1 Pa	1314.02 Pa
Ratio	2.740	1.252	0.935	1.595

Table 7
Total pressure loss in reverse flow mode: inlet Re 6128 condition.

	T - P3	P3 – P2	P2 – P1	P1 - A
Reference	79.74 Pa	8992.53 Pa	53469.9 Pa	1873.91 Pa
New	356.53 Pa	10624.7 Pa	49743.1 Pa	2977.54 Pa
Ratio	4.471	1.182	0.930	1.589

6. Summary

In this study, optimum geometry of the vortex-type fluidic diode for advanced nuclear reactors has been investigated using a

numerical optimization method, and its performance has been evaluated using experimental study and CFD analysis. The vortex-type fluidic diode is a safety-related component proposed in some advanced reactor concepts such as FHR, hybrid-SFR, and etc. This component consists of three main parts; (1) axial port, (2) vortex chamber, and (3) tangential port. In this study, the geometries of the main vortex chamber and the tangential port were taken into considerations while the previous research focused on the axial port.

Topology optimization is a mathematical method that optimizes material distribution in a given design domain. Unlike the conventional shape or size optimization, it does not deal with any predefined design parameters and provide large degree of freedom in geometry and shape. For this reason, the topology optimization is suitable for finding an optimum geometry in the conceptual design level. In this study, the vortex-chamber and the horizontal port has been simplified into 2-D geometry and the topology optimization has been applied for avoiding large computational load and a local minimum issue. As a result, a new chamber and tangential port design has been obtained in which a fin-shape structure was added at the junction between the chamber and the tangential port. Based on this conceptual design, a new vortex type fluidic diode design has been proposed.

In order to validate the concept of the new design, a hydraulic experiment has been conducted. However, the experiment failed to show any significant performance improvement for the new design in comparisons with the original reference design. In addition, as the Re number increased, greater performance degradation was observed. To elucidate the cause of this result, detailed CFD analysis has been applied for the experimental conditions. As a result, it was observed that the major pressure loss occurs in the chamber center and the junction with the tangential port. The loss proportion is 75% for the reference design and as high as 60% for the new design in forward flow and 83% for the reference design and 78% for the new design in reverse flow. The total pressure change in the same subpart for a different design was compared to verify the effect of the design modification in the new design. From a course of 3-D CFD analysis, it could be concluded that the vortex chamber and the tangential port of the fluidic diode have minor contribution on the device performance although these two parts mostly occupy the whole volume. On the other hand, the junction between the vortex chamber and the axial port estimated to be an important contributor to the device performance. Therefore, further studies on this need to be made in the future, and it would lead us to the final optimal design enclosing the whole device.

Acknowledgments

This research was supported by the National Nuclear R&D Program through grants from the National Research Foundation of Korea (NRF) funded by the Ministry of Science ICT & Future Planning (No. 2016M2B2A9911846 and NRF-2013M2B2B1075735).

Nomenclature

D	Tangential Port Diameter [m]
Di	Diodicity
Eu	Euler Number
$\bar{f}_d$	Darcy Friction Force
P	Pressure [Pa]
q	Convexity control parameter
Re	Reynolds Number
$\bar{u}$	Velocity [m/s]
w	Channel width [m]
α	Degree of Impermeability [kg/s·m^3]
α_L	Lower Limit of α [kg/s·m^3]
α_U	Upper Limit of α [kg/s·m^3]
γ	Density Function
ρ	Density [kg/m^3]
μ	Viscosity [kg/m·s]

References

[1] H. Zhang, H. Zhao, C.B. Davis, Thermal Response of the Hybrid Loop-Pool Design for Sodium Cooled Fast Reactors, vol 01, 2008, pp. 1–8.
[2] D.E. Holcomb, S.M. Cetiner, G.F. Flanagan, F.J. Peretz, G.L. Yoder Jr., An Analysis of Testing Requirements for Fluoride Salt Cooled High Temperature Reactor Components, 2009, https://doi.org/10.2172/970926.
[3] G.L. Yoder Jr., Y.M. Elkassabgi, G.I. De Leon, C.N. Fetterly, J.A. Ramos, R.B. Cunningham, Vortex Diode Analysis and Testing for Fluoride Salt-Cooled High-Temperature Reactors, 2012, https://doi.org/10.2172/1036568.
[4] G.H. Priestman, A study of vortex throttles Part 1: experimental, Proc. Inst. Mech. Eng. Part C J. Mech. Eng. Sci. 201 (1987) 337–343, https://doi.org/10.1243/PIME_PROC_1987_201_132_02.
[5] Y. Chikazawa, K. Aizawa, T. Shiraishi, H. Sakata, Experimental demonstration of flow diodes applicable to apassive decay heat removal system for sodium-cooled reactors, J. Nucl. Sci. Technol. 46 (2009) 321–330, https://doi.org/10.1080/18811248.2007.9711537.
[6] A.A. Kulkarni, V.V. Ranade, R. Rajeev, S.B. Koganti, Pressure drop across vortex diodes: experiments and design guidelines, Chem. Eng. Sci. 64 (2009) 1285–1292, https://doi.org/10.1016/j.ces.2008.10.060.
[7] A.A. Kulkarni, V.V. Ranade, R. Rajeev, S.B. Koganti, CFD simulation of flow in vortex diodes, AIChE J. 54 (2008) 1139–1152, https://doi.org/10.1002/aic.11439.
[8] J. Yin, L. Jiao, L. Wang, Large eddy simulation of unsteady flow in vortex diode, Nucl. Eng. Des. 240 (2010) 970–974, https://doi.org/10.1016/j.nucengdes.2010.01.010.
[9] A. Pandare, V.V. Ranade, Flow in vortex diodes, Chem. Eng. Res. Des. 102 (2015) 274–285, https://doi.org/10.1016/j.cherd.2015.05.028.
[10] S. Shin, J.H. Jeong, D.K. Lim, E.S. Kim, Design of SFR fluidic diode axial port using topology optimization, Nucl. Eng. Des. 338 (2018) 63–73, https://doi.org/10.1016/j.nucengdes.2018.07.028.
[11] G.I.N. Rozvany, Aims, scope, methods, history and unified terminology of computer-aided topology optimization in structural mechanics, Struct. Multidiscip. Optim. 21 (2001) 90–108, https://doi.org/10.1007/s001580050174.
[12] T. Borrvall, J. Petersson, Topology optimization of fluids in Stokes flow, Int. J. Numer. Methods Fluids 41 (2003) 77–107, https://doi.org/10.1002/fld.426.
[13] C. Othmer, E. De Villiers, H. Weller, et al., Implementation of a continuous adjoint for topology optimization of ducted flows, 18th AIAA Comput, Fluid (2007) 1–7, https://doi.org/10.2514/6.2007-3947.
[14] S. Lin, L. Zhao, J.K. Guest, T.P. Weihs, Z. Liu, Topology optimization of fixed-geometry fluid diodes, J. Mech. Des. 137 (2015), https://doi.org/10.1115/1.4030297, 081402.
[15] G.H. Yoon, Topology optimization for turbulent flow with Spalart-Allmaras model, Comput. Methods Appl. Mech. Eng. 303 (2016) 288–311, https://doi.org/10.1016/j.cma.2016.01.014.
[16] P.E. Gill, W. Murray, M.A. Saunders, SNOPT: an SQP algorithm for large-scale constrained optimization, SIAM J. Optim. 12 (2002) 979–1006, https://doi.org/10.1137/S1052623499350013.
[17] COMSOL, Opitmization Module User'guide Version 5.1, Comsol, Burlington, MA, USA, 2015.
[18] COMSOL, Optimization of a Tesla Microvalve, Comsol, Burlington, MA, USA, 2015.
[19] M.S. Song, S.H. Park, E.S. Kim, Particle image velocimetry measurements of 2-dimensional velocity field around twisted tape, Fusion Eng. Des. 109–111 (2016) 596–601, https://doi.org/10.1016/j.fusengdes.2016.02.039.
[20] M.S. Song, H.Y. Choi, J.H. Seong, E.S. Kim, Matching-index-of-refraction of transparent 3D printing models for flow visualization, Nucl. Eng. Des. 284 (2015) 185–191, https://doi.org/10.1016/j.nucengdes.2014.12.019.
[21] F.R. Menter, Two-equation eddy-viscosity turbulence models for engineering applications, AIAA J. 32 (1994) 1598–1605, https://doi.org/10.2514/3.12149.
[22] V.C. Patel, W. Rodi, G. Scheuerer, Turbulence models for near-wall and low Reynolds number flows - a review, AIAA J. 23 (1985) 1308–1319, https://doi.org/10.2514/3.9086.
[23] F.S. Lien, W.L. Chen, M.A. Leschziner, Low-Reynolds-Number eddy-viscosity modelling based on non-linear stress-strain/vorticity relations, in: Eng. Turbul. Model. Exp, Elsevier, 1996, pp. 91–100, https://doi.org/10.1016/B978-0-444-82463-9.50015-0.